

---

# Towards Using Cathodoluminescence for 3D Tomography

---

Daphne M. Dekker

*August 8, 2021*

## Supervisors:

M. Liebtrau

Dr. K.W. Mauser

Dr. N.J. Schilder

Prof. dr. A. Polman

Prof. dr. A. Meijerink



**Utrecht University**

## Abstract

A simple structure was designed to investigate whether cathodoluminescence could be used for tomography. The structure consisted of a rectangular hole, with an overhanging tip on one side. Interference was expected from transition radiation produced at the bottom of the hole by the incident electron beam and from radiation at the overhanging tip. It was hypothesised that by measuring the resulting interference pattern, the vertical displacement between these two sources of radiation could be extracted. Several of these structures were fabricated in a monocrystalline gold surface by focused ion beam etching. The angular emission patterns of these structures, that were found by performing angle-resolved cathodoluminescence measurements, showed complex interference patterns, containing many different types of fringes. To understand the origin of these interference fringes, an analytical model was developed that modelled the point of incidence of the electron beam as a source of transition radiation. Transition radiation scattering from the overhanging tip and upper edges of the hole was modelled by a range of closely spaced dipoles placed at positions corresponding to the location of the edges in the structure. The experimental data and the results of the analytical model were found to be in excellent agreement. Therefore it was concluded that interference between transition radiation produced at the bottom of the structure and transition radiation that had been scattered off of the upper edges of the hole was the main contribution to the observed interference fringes in the angular emission patterns. The spacing of the fringes caused by interference of transition radiation scattered off of the overhanging tip with the source transition radiation was found to depend on the depth of the structure and these can therefore be used to find the depth of the hole from the angular emission patterns. This means cathodoluminescence can indeed be used for tomography.

## 1 Introduction

Similarly to how materials can be excited by incident photons and subsequently emit light, materials can also emit light after excitation by electrons. This phenomenon is called cathodoluminescence (CL). Cathodoluminescence can be coherent or incoherent. In the case of coherent CL, there is a phase relation between the electromagnetic field of the incident electron and the emitted light, whereas in incoherent CL there is not. Coherent CL occurs when a material is polarised by the electric field of an electron which couples to a far-field radiation mode. One of the most common types of coherent CL is transition radiation (TR). This takes place when an electron transits an interface between two materials, e.g. an air-metal interface. The electron polarises the interface and this induces radiation similar to that of a vertical dipole. While TR can be relatively weak, or overpowered by incoherent CL mechanisms in some materials, it can be the dominant source of CL in e.g. metals. As electrons generally have very high energies, they are a broadband excitation source. Additionally, because of their high velocity, the polarisation of the interface occurs on very short timescales and therefore induces broadband emission. Besides TR, an electron incident on a surface can also

create surface plasmon polaritons (SPPs). These are guided electromagnetic waves that are confined to the surface and will propagate along this surface until they die out, or encounter some scattering object. [1, 2, 3]

Much like photoluminescence, CL can be used to study optical and electronic properties of materials. Therefore, CL measurements have been used in a number of fields since the second half of 20th century. CL used to be particularly popular in geology, but was not used much in materials science yet. However, recent developments to CL measurement techniques allow for the application of CL measurements to the optical characterisation of nanomaterials with deep-subwavelength resolution. [4] One of these novel techniques is angle-resolved CL measurements, which can be used to find angular emission patterns from samples. In 2020, Schilder et al. used angle-resolved CL measurements to study a silver surface with a silver nanocube on top. By launching electrons at this surface, TR was produced, while SPPs were also launched. These SPPs travelled along the surface until they encountered the nanocube and scattered off of it. Using angle-resolved CL measurements, Schilder et al. were able to find an angular emission pattern that showed interference fringes from interference of the TR and the scattered SPP. From this interference pattern they were then able to find the distance between the point of incidence of the electron beam and the nanocube. [5] The fact that angle-resolved CL measurements can be used to find physical distances in the lateral dimensions of a micro-scaled structure raises the question of whether this can be extended to finding three-dimensional information about a structure from the angular emission pattern. In other words: can cathodoluminescence be used to do tomography?

To answer this question, it needs to be investigated whether angle-resolved CL measurements can be used to find distances in the axial dimension. In order to do this, a zigzag-like structure, as shown in Fig. 1a and b, was used. Light was expected from just two, vertically displaced sources: the point of incidence of the electron beam at the bottom of the structure and the long upper edge, or tip, of the structure. The electron beam might be able to polarise this tip, thereby inducing emission from the tip itself, possibly leading to interference from two distinct sources of CL, as shown in Fig. 1a. Alternatively, the tip might not emit significantly, but interference between these two points might still be observed due to the electron beam producing TR at the bottom of the structure, that can travel towards the tip and scatter off of it, after which the scattered TR can interfere with the source TR in the far-field, as shown in Fig. 1b. In both cases, any interference fringes produced by these two sources would depend on the depth of the structure and the interference pattern is therefore expected to contain information about the vertical displacement of the sources.

## 2 Methods

To fabricate the zigzag-like structure described in the introduction, a FEI Helios Nanolab 600 scanning electron microscope (SEM) equipped with a focused ion beam (Sidewinder Gallium Liquid Metal Ion Source) was used. Using the focused ion beam (FIB) with an ion beam current of 93 pA, a rectangular hole was etched into the surface of a monocrystalline gold disc, that had been cleaned twice using acid piranha and once using base

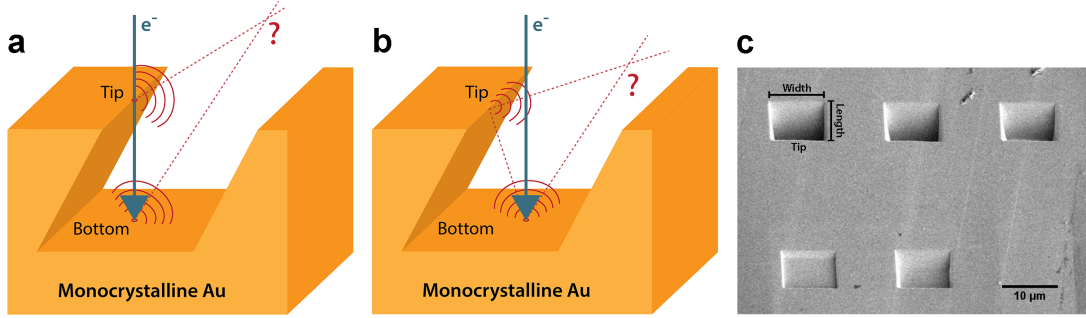


**Figure 1:** Schematic depiction of the structure designed to investigate the possibility of using angle-resolved CL to find the vertical displacement between two structural features. Two possible mechanisms of interference in this structure are (a) excitation of both the tip and the bottom by the same electron beam and (b) TR produced at the bottom of the structure scattering off of the tip and interfering with the source TR. (c) SEM image of several of the structures fabricated by FIB etching. Each of these structures has a different depth.

piranha. The FIB was oriented at a  $52^\circ$  angle with respect to the sample, making two of the walls of the box slanted, thereby creating an overhang, or tip, on one side. Boxes of different sizes were fabricated, with widths ranging from 10 to 25  $\mu\text{m}$  and lengths ranging from 5 to 20  $\mu\text{m}$ . The depth of the boxes was varied by varying the number of passes of the FIB over the designated area. An overview of the settings used can be found in Table 1 in Appendix A. An SEM image of several of the fabricated structures, all with different depths, is shown in Fig. 1c.

Angle-resolved cathodoluminescence measurements on these structures were performed in a FEI Quanta FEG 650 SEM equipped with a Schottky field emission electron source using an accelerating voltage of 30 keV. CL was collected using a half-parabolic mirror. Each point on this mirror corresponds to a specific set of zenithal and azimuthal angles, which enables the collection of angular emission patterns. A small hole in the top of the mirror allows the electron beam to reach the sample. The sample was oriented in such a way that the tip faced the apex of the mirror for optimal collection of CL from the tip and from inside of the structure. The mirror reflects the collected CL out of the SEM chamber and into a Delmic Sparc Spectral system, which contains optics that focus the collected light onto a CCD camera. The measurements were performed using several different bandpass filters with central wavelengths of 500, 550 nm and 650 nm, all with a bandwidth of 40 nm. Angle-resolved emission patterns were recorded with the electron beam parked in one specific position on the sample for 30 - 90 s. For each structure, a range of measurements with the electron beam at different positions on the sample was performed. The positions were chosen in a line perpendicular to the tip with a step size of 230 nm, from a point on the upper surface of the structure to a point on the other side of the tip, where the electron hits the bottom of the structure. Additional experimental parameters can be found in Table 2 in Appendix A.

Besides angle-resolved CL measurements, hyperspectral CL measurements were also

performed. Contrary to angle-resolved measurements, in hyperspectral measurements CL from only one azimuthal angle but from a large range of wavelengths is collected. The azimuthal angle was selected by inserting a slit of  $200\ \mu\text{m}$  into the system, and the collected CL was first directed to a  $300\ \text{l/mm}$  (blaze:  $500\ \text{nm}$ ) grating before being sent to a CCD camera. In that way, CL with wavelengths from  $378$  to  $821\ \text{nm}$  from all zenithal angles was recorded. The electron beam was scanned over the tip in a line perpendicular to the tip with a step size of  $230\ \text{nm}$  and the beam being parked in each position for  $300\ \text{s}$ .

### 3 Results and Discussion

#### 3.1 Angle-resolved measurements

Angular CL emission patterns were obtained as described in the previous section. Fig. 2a shows the angular emission pattern acquired from measurements on a box of  $9.88$  by  $4.33\ \mu\text{m}$  that was approximately  $1.2\ \mu\text{m}$  deep. The electron beam was placed approximately  $10\ \text{nm}$  away from the tip, i.e. just passing by the tip and impacting onto the bottom surface of the structure. The straight cut off on the bottom of the pattern corresponds to the opening of the mirror. The dark spot in the pattern, observed where both  $k_x/k_0$  and  $k_y/k_0$  are zero, shows the position of the hole in the top of the mirror that the electrons pass through. Thus, this region of the image shows light travelling directly upwards from the sample, while the upper region of the image corresponds to light collected at the apex of the mirror. Since the opening of structure is oriented towards the apex, any radiation from the structure is predominantly expected in this region of the pattern. In this region, the angular emission pattern indeed shows several types of clearly resolved interference fringes. Closely spaced vertical fringes are visible, along with closely spaced, slightly curved horizontal fringes, that lead to a square-like interference pattern in the middle of the image. Additionally, bright, larger features are observed near the edges of the image.

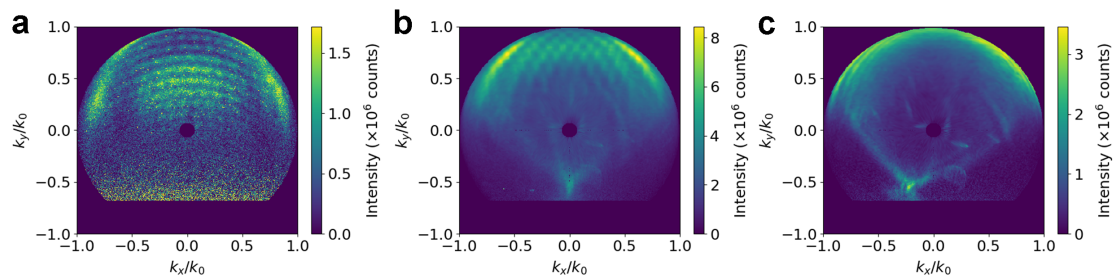


**Figure 2:** Angular emission patterns acquired from three different boxes with different dimensions: (a) a small box of  $9.88$  by  $4.33\ \mu\text{m}$  and  $1.2\ \mu\text{m}$  deep, (b) a narrow box of  $10$  by  $20\ \mu\text{m}$  and  $1.8\ \mu\text{m}$  deep and (c) a larger box of  $25$  by  $20\ \mu\text{m}$  and  $1.8\ \mu\text{m}$  deep. The electron beam was approximately  $10\ \text{nm}$  away from the tip in all three measurements.

To gain more insight into the origin of the different types of fringes in this complex interference pattern, angle-resolved CL measurements were performed on boxes with

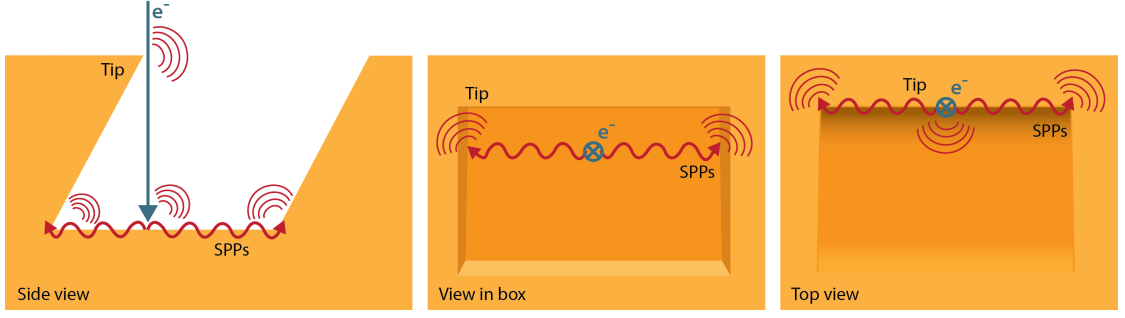


**Figure 3:** Schematic depiction of several scattering mechanisms that could occur when the electron beam launches SPPs in the structure.

several different dimensions. Fig. 2b shows the angular emission pattern acquired from a narrow box of 10 by 20 by 1.8  $\mu\text{m}$ . The width of this narrow box is similar to the width of the box discussed previously, while the length is significantly increased. The curved fringes observed for the smaller box are not observed in the emission pattern from the narrow box. The larger fringes near the edges are still clearly visible, as is the square-like interference pattern, albeit shifted upwards somewhat. Angle-resolved measurements were also performed on a larger box of 25 by 20 by 1.8  $\mu\text{m}$  and the acquired emission pattern is shown in Fig. 2c. Contrary to the emission patterns from the smaller and the narrow boxes, the emission pattern of this larger box does not show the square-like interference pattern; only the larger, bright fringes just at the edge of the image are clearly discernible. The difference between these three emission patterns indicates that the interference patterns are not caused solely by interference from radiation at the tip and the bottom of the structure, but that scattering of light from the other edges in the structure also contributes to the overall interference pattern. Several scattering mechanisms are possible. TR produced by the incident electron beam on the bottom of the structure could be scattering off the edges of the box. As schematically depicted in Fig. 3, the electron can also launch SPPs on the bottom of the structure, that possibly scatter off the long and short edges of the structure. Additionally, the electron beam might be launching SPPs on the tip itself, that can travel along the tip and scatter off the corners. Because interference between radiation from the tip and the bottom is the main focus of this study, all further experiments were performed on broad boxes of 25 by 10  $\mu\text{m}$ , to try to eliminate the contribution from the other edges in the structures.

The results of angle-resolved CL measurements on three boxes of 25 by 10  $\mu\text{m}$ , each with a different depth are shown in Figures 4a-c, a being the most shallow structure and c being the deepest structure. The electron beam was placed at approximately 1  $\mu\text{m}$  away from the tip in each of these measurements. All three images show mainly two types of interference fringes: closely spaced curved fringes, which are similar to the fringes that were observed in Fig. 2a, and the much larger fringes closer to the edge of the pattern. When comparing the patterns for the three different depths, the spacing of the curved fringes remains relatively constant with varying depth. However, the number of the larger fringes, and consequently the spacing of these fringes, changes significantly with changing depth. It is observed that the spacing of the large fringes decreases as the



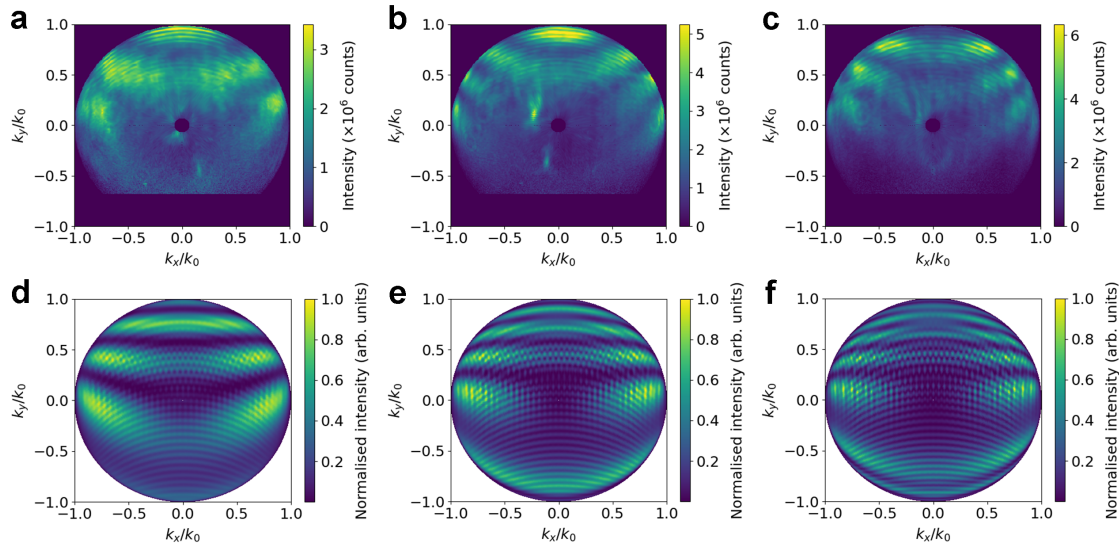


**Figure 4:** (a-c) Experimentally obtained angular emission patterns from boxes of 25 by 10  $\mu\text{m}$  and a depth of (a) 0.9  $\mu\text{m}$ , (b) 1.8  $\mu\text{m}$  and (c) 2.7  $\mu\text{m}$ . (d-f) Angular intensity patterns obtained using the analytical model. The parameters in the model correspond to a geometry of 25 by 10  $\mu\text{m}$ , with depths of (d) 0.9  $\mu\text{m}$ , (e) 1.8  $\mu\text{m}$  and (f) 2.7  $\mu\text{m}$ . The electron beam was placed at approximately 1  $\mu\text{m}$  from the tip in all six images.

depth of the hole increases. This observation matches with what would be intuitively expected, when considering that smaller distances in k-space correspond to larger distances in real space.

Similarly, it was investigated how the interference fringes depended on the radial distance between the tip and the electron beam. Fig. 5a-c show the angular emission patterns acquired from a box of 25 by 10 by 1.8  $\mu\text{m}$  for different positions of the electron beam. In Figure 5a, the electron beam was approximately 1  $\mu\text{m}$  away from the tip and it was moved 230 nm closer to the tip in each subsequent image. No strong change is observed for the small curved fringes when the position of the electron beam is changed. However, the number of larger fringes near the edge of the pattern and their spacing does change as the radial distance between the tip and the electron beam is varied. As the distance between the tip and the electron beam decreases, the number of fringes also decreases and therefore the spacing of the fringes increases. This again corresponds well to the expectations based on the concept of smaller distances in real space translating to larger distances in k-space.

The distance from the tip to the point of incidence of the electron beam on the bottom depends on both the depth of the structure and the position of the electron beam. The strong dependence of the number and spacing of the larger interference fringes on both of these parameters is a strong indication that these larger fringes originate from interference between radiation at the tip and radiation at the bottom of the structure. In the introduction it was hypothesised that the tip itself might radiate after excitation by the electron beam (Fig. 1a). However, the large fringes are still observed when the

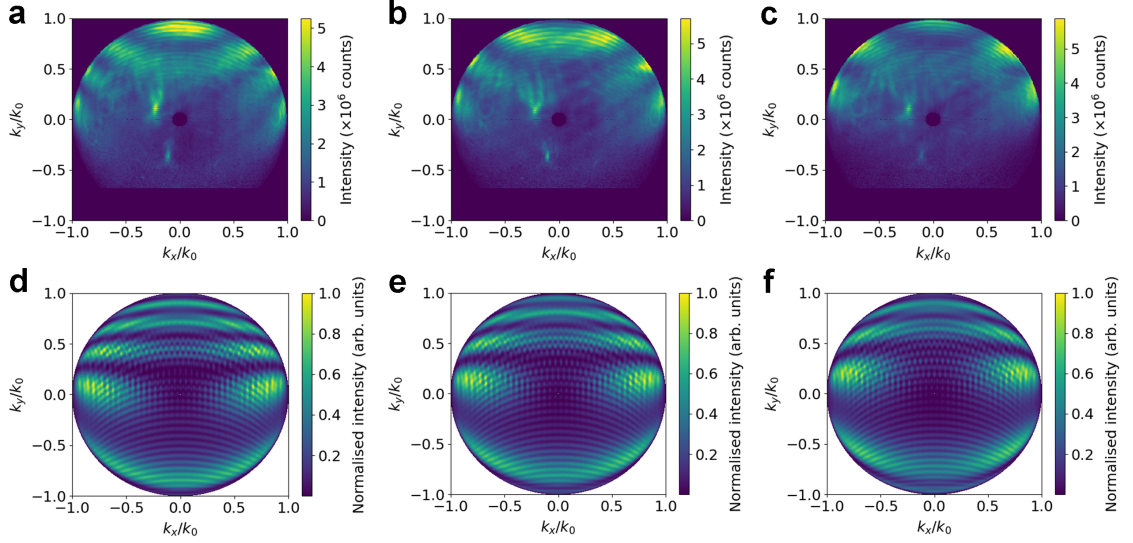


**Figure 5:** (a-c) Experimentally obtained angular emission patterns from boxes of 25 by 10  $\mu\text{m}$  and a depth of 1.8  $\mu\text{m}$ . The electron was placed at approximately (a) 1.02  $\mu\text{m}$ , (b) 0.79  $\mu\text{m}$  and (c) 0.56  $\mu\text{m}$  away from the tip. (d-f) Angular emission patterns obtained using the analytical model. The parameters in the model correspond to a geometry of 25 by 10  $\mu\text{m}$  with a depth of 1.8  $\mu\text{m}$ , where the position of the electron beam with respect to the tip was (d) 1.02  $\mu\text{m}$ , (e) 0.79  $\mu\text{m}$  and (f) 0.56  $\mu\text{m}$ .

electron beam is a micron away from the tip. It is unlikely that the tip is excited by the electron beam at that distance. Therefore, it is more likely that the most dominant source of radiation at the the tip is TR that was produced at the bottom of the structure and scatters off of the tip. The large fringes are expected to be caused by interference between this scattered TR at the tip and the source TR produced at the bottom of the structure.

### 3.2 Analytical model

To investigate the validity of the hypothesis stated above, an analytical model was developed. In this model, the electron beam incident on the bottom surface of the structure was modelled by one source of transition radiation, which was defined to be in the origin of the system. The radial and axial electric field components of TR are given by the following equations, which were based on expressions reported by F. Javier García de Abajo et al. and B.J.M. Brenny et al. [6, 7],

$$\mathbf{E}_{\text{TR}}^{\text{rad}}(\mathbf{r}) = \frac{1}{4\pi\epsilon_0} ik_0 \cos\theta D\mu_1 \frac{e^{ik_0|\mathbf{r}|}}{|\mathbf{r}|} \cos\theta \quad (1)$$

$$\mathbf{E}_{\text{TR}}^{\text{ax}}(\mathbf{r}) = \frac{1}{4\pi\epsilon_0} ik_0 \cos\theta D\mu_1 \frac{e^{ik_0|\mathbf{r}|}}{|\mathbf{r}|} \sin\theta \quad (2)$$



where  $\varepsilon_0$  is the vacuum permittivity,  $k_0 = 2\pi/\lambda$  is the wavenumber, with  $\lambda$  being the free space wavelength,  $\theta$  is the emission angle and  $\mathbf{r}$  is the vector pointing from the source to the point of observation.  $D$  in this equation is given by

$$D = \frac{2ieQ/c}{\varepsilon_1 q_{z2} + \varepsilon_2 q_{z1}}, \quad (3)$$

where  $Q = k_0 \sin \theta$  is the parallel wave vector component,  $c$  is the speed of light in vacuum, and  $\varepsilon_1$  and  $\varepsilon_2$  are the dielectric constants of air and gold, respectively. The perpendicular wave vector components in medium 1 and medium 2,  $q_{z1}$  and  $q_{z2}$ , are given by Eq. 4.

$$q_{zj} = \sqrt{k_0^2 \varepsilon_j - Q^2} \quad (4)$$

Finally, the function  $\mu_1$  in Eq. 1 and 2, is given by

$$\mu_1 = \frac{\varepsilon_1 q_{z2} - \varepsilon_1 \omega/v}{q^2 - k_0^2 \varepsilon_2} - \frac{\varepsilon_1 q_{z2} - \varepsilon_2 \omega/v}{q^2 - k_0^2 \varepsilon_1}, \quad (5)$$

where  $\omega$  is the angular frequency of the emission,  $v$  is the electron velocity, and  $q = \sqrt{Q^2 + (\omega/v)^2}$  is the wavenumber of each plane wave, which in this case is not necessarily equal to the free space wavenumber, because our incident field is bound to deep-subwavelength matter, an electron.

The TR scattering off of the upper rim of the structure was modelled by a range of closely spaced dipoles, each with a set of coordinates that correspond to a point on one of the edges in the structure used for the experiments. We assume that both the radial and axial field components of the TR are scattered by the structure. Therefore, two orthogonal dipoles were placed at each point, one corresponding to the scattering of the radial field component of the source TR and one corresponding to the scattering of the axial field component. The electric field components of a dipole induced by the radial field component of the TR is given by the following equations,

$$\mathbf{E}_{D,\text{rad}}^{\text{rad}}(\mathbf{r}) = \mu_0 \omega^2 \frac{\cos \theta}{4\pi |\mathbf{r} - \mathbf{r}_0|} P_{\text{rad}}(\mathbf{r}_0) e^{i(k_0 |\mathbf{r} - \mathbf{r}_0| + \varphi_0)} \cos \theta \quad (6)$$

$$\mathbf{E}_{D,\text{rad}}^{\text{ax}}(\mathbf{r}) = \mu_0 \omega^2 \frac{\cos \theta}{4\pi |\mathbf{r} - \mathbf{r}_0|} P_{\text{rad}}(\mathbf{r}_0) e^{i(k_0 |\mathbf{r} - \mathbf{r}_0| + \varphi_0)} \sin \theta \quad (7)$$

and the equations for the electric field components of a dipole induced by the axial field component of the TR read as follows

$$\mathbf{E}_{D,\text{ax}}^{\text{rad}}(\mathbf{r}) = \mu_0 \omega^2 \frac{\sin \theta}{4\pi |\mathbf{r} - \mathbf{r}_0|} P_{\text{ax}}(\mathbf{r}_0) e^{i(k_0 |\mathbf{r} - \mathbf{r}_0| + \varphi_0)} \cos \theta \quad (8)$$

$$\mathbf{E}_{D,\text{ax}}^{\text{ax}}(\mathbf{r}) = \mu_0 \omega^2 \frac{\sin \theta}{4\pi |\mathbf{r} - \mathbf{r}_0|} P_{\text{ax}}(\mathbf{r}_0) e^{i(k_0 |\mathbf{r} - \mathbf{r}_0| + \varphi_0)} \sin \theta. \quad (9)$$

The sum of Eq. 6 and 8 equals the total radial electric field component of each dipole. Equivalently, the sum of Eq. 7 and 9 gives the total axial electric field component. In these expressions,  $\mu_0$  is the vacuum permeability and  $\omega$  is the angular frequency of the emission. The term  $\mathbf{r}_0$  is the vector pointing from the source TR towards the scattering

dipole and therefore contains the coordinates of each dipole. The phase term  $\varphi_0$  can be used to include a scattering phase offset, e.g.  $\pi$ , which would correspond to the phase offset after reflection on a perfect mirror. The scattering phase offset was set to 0 in this study, but its value could be optimised to further improve the accuracy of the model. The terms  $P_{\text{rad}}(\mathbf{r}_0)$  and  $P_{\text{ax}}(\mathbf{r}_0)$  are the induced radial and axial polarisation densities of the dipole by the TR and are given by

$$P_{\text{rad}}(\mathbf{r}_0) = 3\varepsilon_0 d \sigma \mathbf{E}_{\text{TR}}^{\text{rad}}(\mathbf{r}_0) \quad (10)$$

$$P_{\text{ax}}(\mathbf{r}_0) = 3\varepsilon_0 d \sigma \mathbf{E}_{\text{TR}}^{\text{ax}}(\mathbf{r}_0), \quad (11)$$

where  $\varepsilon_0$  is the vacuum permittivity,  $d$  is the spacing between the dipoles, which should always be several times smaller than the emission wavelength, and  $\sigma$  is an effective scattering cross section of the dipole.  $\mathbf{E}_{\text{TR}}^{\text{rad}}(\mathbf{r}_0)$  and  $\mathbf{E}_{\text{TR}}^{\text{ax}}(\mathbf{r}_0)$  are the radial and axial field components of the TR, evaluated at the position of the scattering dipole. Including this term in the model ensures that scattering dipoles that are further away from the source TR contribute to the interference pattern less than scattering dipoles that are in close proximity to the source TR do.

The angular intensity pattern for this model system can be calculated from the sum of the electric fields of all the scattering dipoles positioned on the edges and the electric field of the TR, evaluated at the point of observation  $r$ , as shown in Eq. 12.

$$I(\mathbf{r}) = \frac{\varepsilon_0 c}{2} \left| \mathbf{E}_{\text{TR}}(\mathbf{r}) + \sum_i \mathbf{E}_{\text{D},i}(\mathbf{r}) \right|^2 \quad (12)$$

The intensity patterns found using the equations described above could be directly compared to the angular emission patterns that were obtained experimentally. Fig. 4a-c shows the angular emission patterns from three boxes with different depths, as described previously. Fig. 4d-f show the results of the analytical model for corresponding geometries. Many similarities between the experimental data and the model can be observed, e.g. in Fig. 4a and d. The result of the model shows closely spaced curved fringes, very similar to the ones observed in experiment. Additionally, the simulated intensity pattern shows square-like fringes that closely resemble the fringes that were observed for some more narrow geometries (Fig. 2a, b). The model also shows large, bright fringes closer to the edge of the pattern. The number of these large fringes corresponds well to the number of large fringes observed in experiment. Additionally, the variation of the number and spacing of the large fringes as observed in the model depends on the depth of the box in the same way as was observed in the experiment. The similarities between the types of fringes found in the model and in the experimental data, and the similar trend with varying depth of the structure observed in both, indicate good agreement between the model and the experiment.

There is a discrepancy between the curvature of the large fringes in the model and the experiment. A possible explanation for this could be that the experimental data shows slight aberrations, due to the fact that the parabolic mirror was aligned in such

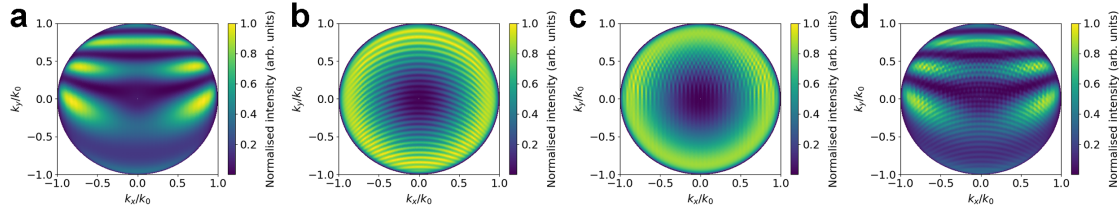


**Figure 6:** Angular intensity patterns that show the results of the analytical model when a range of scattering dipoles is included (a) only along the tip, (b) only along the edge opposite the tip, (c) along both of the shorter edges of the structure and (d) along all the edges of the box. These results were obtained for a geometry corresponding to a box of 25 by 10  $\mu\text{m}$  that is 0.9  $\mu\text{m}$  deep, where the radial distance between the tip and the electron beam is 1.02  $\mu\text{m}$ .

a way that TR from the upper surface of the structure is in focus, while it is now likely that the TR predominantly originates from the bottom of the structure, 1 to 2  $\mu\text{m}$  below the focus of the system. To further investigate this in the future, an aberration term could be added to the model.

A similar comparison between model and experiment was performed for the data set showing the variation of the interference pattern with varying electron beam position, as shown in Fig. 5. A comparison between the upper and bottom row of this figure shows that the large fringes observed in the simulated emission patterns change with varying radial distance between the electron beam and the tip in the same way the large fringes in the experimental data do, i.e. the spacing between the fringes increases as the radial distance between the tip and the electron beam decreases. Since the analytical model was based solely on the scattering of TR off of the edges in the structure, the excellent agreement between the experimental data and the results of the model strongly indicates that the main contribution to the interference patterns observed in the experiment is indeed interference between TR scattered off the edges of the structure and the source TR produced at the bottom of the structure.

The model can also be used to investigate from which edges in the structures specific types of fringes originate. By including only dipoles with coordinates corresponding to the location of one specific edge in the structure, the contribution from this edge to the overall interference pattern can be investigated. Fig. 6a shows the result of the model for scattering dipoles being placed only along the tip. This interference pattern shows only the large fringes, that are known to depend on the depth of the structure and the position of the electron beam. This indicates that the large fringes are indeed due to interference from scattered TR from the tip and TR produced at the bottom of the structure, and thus contain information about the distance between the point of incidence of the electron beam and the tip. Fig. 6b shows the model's result for dipoles placed only along the edge opposite the tip. This image shows closely spaced curved fringes, similar to the curved fringes observed in many of the experimentally obtained emission patterns. It is therefore likely these fringes can be attributed to the interference between the source TR and the TR scattering off of the far edge of the box. The model

was also used to find the contribution from the short edges of the box and the result is shown in Fig. 6c. This image shows a small, square-like interference pattern that closely resembles the pattern observed in several narrow geometries, as shown in e.g. Fig. 2b. This indicates that these fringes originate from interference between the source TR and TR scattered off of the shorter edges of the structure. An interesting feature to note in Fig. 6b and c is the bright, broad ring of intensity. This is the characteristic shape of TR. The fact that the source TR is clearly visible in these emission patterns, while it is not in Fig. 6a, visualises that the scattering off of the edges of the box that are further away from the source contributes less to the overall interference pattern than scattering off of nearby edges does. Fig. 6d reiterates what was shown before; when scattering dipoles are included along all the edges in the analytical model, the observed results strongly resemble the experimentally acquired angular emission patterns.

### 3.3 Hyperspectral measurements

As mentioned in the Methods section, besides angle-resolved CL measurements, hyperspectral CL measurements were also performed. In these measurements, CL is collected from only one azimuthal angle, but for a large range of wavelengths. The data from such measurements can contain information about the nature of the radiation in the system. This data might therefore be used, for example, to find out whether only TR occurs in the system, or whether e.g. SPPs also play a role. An example of a data set acquired from a hyperspectral measurement is included in Fig. 7. The results of these measurements are preliminary and no in depth analysis of the data has been performed yet. Each of the different panels in Fig. 7 corresponds to a different position of the electron beam. The approximate radial distance between the tip and the electron beam is given in the top left corners, where positive numbers correspond to the electron beam passing by the tip and impacting on the bottom of the structure, while negative numbers correspond to the electron beam being placed on the other side of the tip and impacting directly onto the upper surface of the structure. Since only one azimuthal angle is observed in these measurements, a horizontal slice of these hyperspectral images corresponds to a vertical slice at  $k_x/k_0$  is zero of an angular emission pattern for a specific wavelength. The dark spot observed in angle-resolved maps due to the hole in the mirror that allows the electron beam through is therefore observed as a dark line in these images.

Many different features can be observed in all panels. The curvature of the thin diagonal lines might contain information about any plasmonic contribution to the radiation in the system. The origin and significance of the dark, larger diagonal features are not yet understood. However, extending the analytical model to simulate hyperspectral measurements might be able to help in understanding these features. The results obtained on opposite sides of the tip differ significantly from one another. A comparison between the two might deliver new insights into the mechanisms at play in the structure, e.g. at the tip itself. As mentioned previously, this data is preliminary and should be further analysed in future studies.

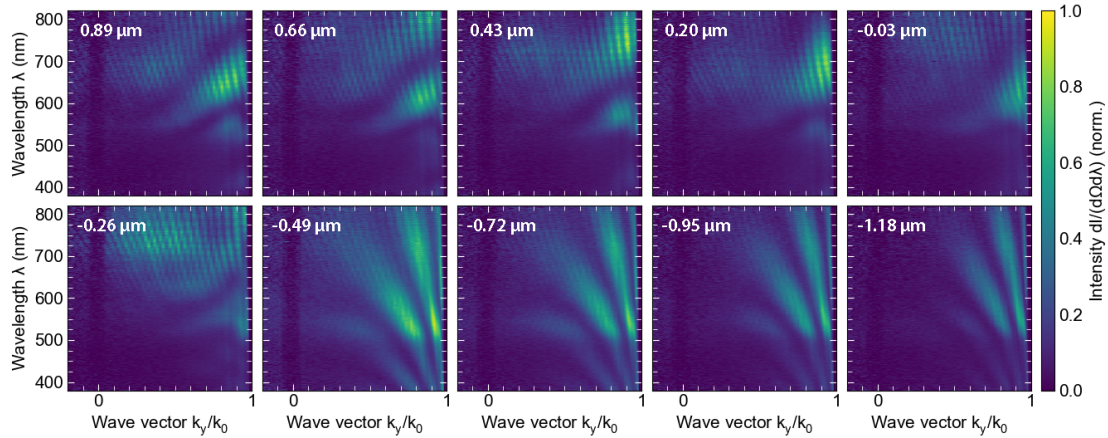


**Figure 7:** *Intensity patterns acquired by performing hyperspectral CL measurements on a structure of 25 by 10  $\mu\text{m}$  with a depth of approximately 1.8  $\mu\text{m}$ . The different panels correspond to data obtained at different electron beam positions.*

## 4 Conclusion

To investigate the question of whether CL measurements can be used to do tomography, a zigzag-like structure, like the one shown in Fig. 8, was designed. In this structure, interference was expected between radiation at a point on the bottom of the structure and radiation at the tip, which could either be light emitted by the tip itself, or TR scattering off of the tip. A number of such structures, with varying lateral dimensions and depths, was fabricated by etching rectangular holes into a monocrystalline gold surface using a FIB oriented at a  $52^\circ$  angle with respect to the sample. By performing angle-resolved CL measurements on these structures, angular emission patterns showing a number of different interference fringes were obtained. The complexity of the emission patterns indicated that several different sources of radiation were present in the system. Besides any radiation from the tip and the TR radiation produced at the bottom of the structure, TR or SPPs scattering off of the long and short edges of the box were therefore hypothesised to contribute to the overall interference pattern.

To investigate the origin of the interference fringes, an analytical model was developed. The electron beam incident on the bottom of the structure was modelled by a single source of TR. A range of closely spaced dipoles, each with a set of coordinates corresponding to a position on the upper edge of the structure, was used to model the source TR scattering off of this edge. The simulated angular intensity patterns showed interference fringes that strongly resembled the interference patterns observed in experiment. The variation of the number and spacing of the interference fringes with changing depth and radial distance between the tip and the electron beam was also very similar to the trends found in the experimental data. The excellent agreement between the experimental data and this analytical model indicates that interference between the source TR produced at the bottom of the structure and TR scattered off of the upper edge of the structure is the main contribution to the observed interference patterns, as schematically depicted in Fig. 8. While scattered TR is likely the most dominant contribution

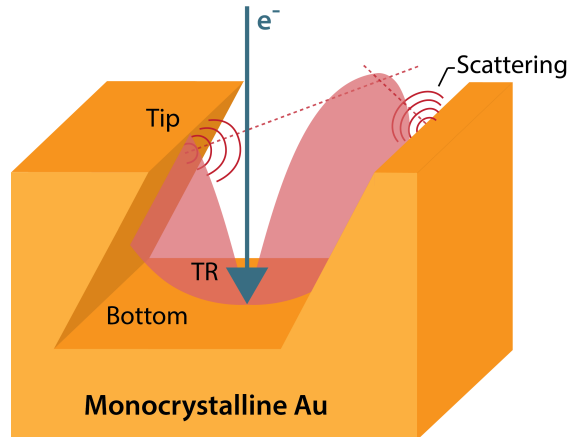


**Figure 8:** *Schematic depiction of the dominant mechanism contributing to interference fringes found in the angular emission patterns. The short edges of the structure are omitted for simplicity here, but scattering off of these edges does contribute the interference patterns.*

to the emission pattern, this does not exclude some, possibly small, contributions due to scattering of SPPs and emission from the tip itself. The results of hyperspectral CL measurements performed on the same structures might be able answer this remaining question in future studies.

The analytical model was also used to find the origin of each of the different types of interference fringes. One of the types of fringes was found to be caused by interference between the source TR and the TR scattered off of the tip. The spacing of these fringes depends directly on the distance between the tip and the point of incidence of the electron beam on the bottom of the structure. These fringes therefore contain information about the depth of the structure, which can thus be extracted from the angular emission patterns. This means that it is indeed possible to use angle-resolved CL measurements to find distances in the axial dimension and therefore that CL measurements can be used to do three-dimensional tomography. Using CL to do tomography can be interesting, because using an electron beam allows for significantly smaller probe sizes than can usually be achieved when using light and optics. Additionally, many tomography methods depend on tilting of the sample, which results in long acquisition times and introduces the missing-wedge problem. Angle-resolved measurements are relatively fast and no tilting is required, which can help circumvent these problems. Furthermore, the method reported by Schilder et al. that was mentioned in the Introduction, where interference from TR and scattered SPPs is used to find dimensions of a structure, relies on the propagation of SPPs and therefore depends strongly on the properties of the materials in the structure. The method reported in this work depends only on the propagation of TR through free space and can therefore be more widely applicable.



## 5 Outlook

As mentioned previously, the data acquired from hyperspectral CL measurements has not been analysed yet. It is important to do so in the future, as this data might contain many new insights about the mechanisms at play in the structure and will lead to a more complete understanding of our system. Any new insights gathered from the hyperspectral data should be used to refine the analytical model, to further improve the agreement between the model and the experiment. This improved model might then be used to extract the depth of our structures from the angular emission patterns, by fitting the model to the experimental data and extracting the depth for which the model and data are most alike.

Subsequently, it should be tested to what extent this method can be used to do tomography. To do this, angle-resolved CL measurements can be performed on the same type of structure, but with unknown width, length and depth. As a next step, measurements should be performed on structures of which no a priori information about the geometry is available. Structures consisting of several different materials and containing buried geometries should be considered as well, because if angle-resolved CL measurements can be used to do tomography on buried structures, this method would be very interesting for e.g. chip fabrication.

Besides information about the geometry of the structure, this experiment might also be able to give us insights into the nature of the incident electron itself. This concerns the question of whether an electron acts as a point charge or as a wavepacket. The phase offset between two sources of radiation, and therefore their interference pattern, depends on the distance the electron has to travel between the two points. In case of electrons acting as a point charge, the distance between the excitation point at the tip and at the bottom would be exactly the same for each electron, whereas in the case of electrons acting as a wavepacket, the effective distance between the two sources can vary slightly between each electron. In the latter case, any interference fringes are likely to be more smeared out than in the case of electrons behaving as a point charge. To do this experiment, two coherent sources of radiation are necessary, which means the tip and the bottom should be excited by the same electron and the tip itself should be emitting. Because the tip was not observed to emit strongly in the current geometry, a resonant structure, e.g. a nanowire, could be placed on the tip, to ensure two vertically displaced coherent sources of emission. Alternatively, the structure could be covered by a thin film of a transparent material that emits bright TR, like silica. Comparing the angular emission patterns of these altered structures to the emission patterns acquired in the current study might be able to shed some light onto the nature of the behaviour of the electrons in the system.

## 6 Acknowledgements

While working on this project for the past five months, I have learned more about cathodoluminescence, the electric field of dipoles and interference patterns than I ever thought I would. None of that would have been possible without all of the people who

helped me along the way, so I would like to thank them here.

First of all, I want to thank Kelly. When I arrived at AMOLF, I did not know anything about this subject yet and you really took the time to teach me all the basics and all the details I needed to know. Thank you for being so patient with me, for always making time to help me and for making me feel at home at AMOLF right away with your kindness, but more importantly with your slightly dark sense of humour!

Secondly, I want to thank Matthias. I really appreciate you always making time for lengthy and really helpful discussions about the interpretation of my data and the development of the analytical model, even when you were incredibly busy yourself. I want to thank you for this time investment, for being a great teacher, who even taught me some German here and there, and for providing delicious snacks during the long waiting times of late night experiments!

Nick, I want to thank you for all of your help with the development of the analytical model. Whenever Matthias and I got stuck somewhere, you were always able to help us figure it out. I am very grateful that, while you have a full time job, you still took the time to have weekly meetings with us. I cannot thank you enough!

I want to thank Igor for fabricating all the structures used in this study and for the fun conversations during fabrication. I also want to thank you, along with Bob and Dimitry, for putting a lot of effort into cleaning the gold sample.

I want to thank Andries, for advising me on how to find a place to do my internship and for being willing to be involved with this project as my second supervisor.

I am incredibly grateful to Albert for giving me the opportunity to do my internship in his group. I was really impressed when on my very first day at a new research group, the group leader made time to have a chat with three young women to talk about what it is like to be a woman in science. Thank you for always being very involved in the project, but also in me as a person and giving me advice about how to decide what to do after university. Thank you very much for your supervision and for making the Photonic Materials group such a great environment.

Last but certainly not least, I want to thank everyone else in the Photonic Materials group. Andrea, Evelijn, Heleen, Magda, Nika, Stefan, Tom, Verena, and of course the people mentioned previously, all of you made me feel welcome in the group from my very first day. I love how close this group is and that even during a pandemic you find ways to spend time together. Thank you all so much for making my time here as enjoyable as it was!

## References

- [1] T. Coenen, *Angle-resolved cathodoluminescence nanoscopy*. PhD thesis, University of Amsterdam, Amsterdam, 5 2014.
- [2] B. Brenny, *Probing light emission at the nanoscale with cathodoluminescence*. PhD thesis, University of Amsterdam, Amsterdam, 6 2016.
- [3] M. Magdalena Solà Garcia, *Electron-matter interaction probed with time-resolved cathodoluminescence*. PhD thesis, University of Amsterdam, Amsterdam, 7 2021.
- [4] T. Coenen and N. M. Haegel, “Cathodoluminescence for the 21st century: Learning more from light,” *Applied Physics Reviews*, vol. 4, p. 031103, 9 2017.
- [5] N. J. Schilder, H. Agrawal, E. C. Garnett, and A. Polman, “Phase-Resolved Surface Plasmon Scattering Probed by Cathodoluminescence Holography,” *ACS Photonics*, vol. 7, pp. 1476–1482, 6 2020.
- [6] F. J. García De Abajo, “Optical excitations in electron microscopy,” *Reviews of Modern Physics*, vol. 82, pp. 209–275, 2 2010.
- [7] B. J. M. Brenny, A. Polman, and F. J. G. d. Abajo, “Femtosecond plasmon and photon wave packets excited by a high-energy electron on a metal or dielectric surface,” *Physical Review B*, vol. 94, p. 155412, 10 2016.

## Appendices

### A Experimental settings

**Table 1:** *Settings used for fabrication of the structures using focused ion beam etching.*

	Small structures	Large structures
<b>Ion beam current</b>	93 pA	93 pA
<b>Ion dose</b>	1.93 nC/ $\mu\text{m}^2$	329.96 pC/ $\mu\text{m}^2$
<b>Dwell time</b>	1 $\mu\text{s}$	1 $\mu\text{s}$
<b>Pitch</b>	10.8 nm	15 nm
<b>Overlap</b>	55%	37.5%
<b>Scan type</b>	Serpentine	Serpentine



---

```

eps0 = 8.854e-12          # vacuum permittivity in
mu0 = 4*pi*1e-7          # vacuum permeability in
hbar = 6.582119514e-16   # Plank's constant in eV*s

# define electron parameters
Ekin = 30*keV             # electron kinetic energy in eV
E = m0 + Ekin             # total electron energy in eV
v = sqrt(1-(m0/E)**2)*c   # electron velocity in m/s

# define optical field parameters
wl = 650*nm               # emission wavelength in m

# define geometrical box parameters
wx = 25*um               # width of box in m
wy = 10*um               # length of box in m
hz = 0.9*um              # depth of box in m
dx = 12.5*um             # distance in x direction of left
                           # side to ebeam in m
dy = 1.02*um             # distance in y direction of front
                           # edge to ebeam in m

# define scattering dipole parameters
sigma = (200*nm)**2       # scattering cross section

%%
spacing = 50*nm
Nx = int(wx/spacing)+1
Ny = int(wy/spacing)+1
Nth = 600
Nph = 600

theta = np.linspace(0., pi/2., Nth)
phi = np.linspace(0., 2*pi, Nph)

x = np.concatenate([np.linspace((wx-dx),(wx-dx),Ny),np.linspace((wx-dx),
    -dx,Nx),np.linspace(-dx,-dx,Ny),np.linspace(-dx,(wx-dx),Nx)])
y = np.concatenate([np.linspace((wy-dy),-dy,Ny),np.linspace(-dy,
    -dy,Nx),np.linspace(-dy,(wy-dy),Ny),np.linspace((wy-dy),(wy-dy),Nx)])
d = y[1] - y[0]
N = np.size(x)

%% Definition Au dielectric function from linear interpolation of
tabulated data (Johnson & Christy 1972)

def epsAu(w):

    # input parameter:
    # w = emission angular frequency in 1/s

    eps_tab = 'eps_Au_JohnsonChristy1972.txt'
    data = open(eps_tab,'r')

    ws = []
    epsRe = []
    epsIm = []

```

---

```

for i, line in enumerate(data):
    if i > 7:
        # photon energy sample in eV
        E = float(line.rstrip().split()[0])

        # angular frequency sample in 1/s
        ws.append(E/hbar)

        # dielectric constant sample (real part)
        epsRe.append(float(line.rstrip().split()[1]))

        # dielectric constant sample (imaginary part)
        epsIm.append(float(line.rstrip().split()[2]))

# angular frequency samples in 1/s
ws = np.asarray(ws)

# dielectric constant samples
eps = np.asarray(epsRe) + 1j*np.asarray(epsIm)

# interpolation function
epsInt = interp1d(ws, eps)
return epsInt(w)

%% Definition of transition radiation (source field)
def E_TR(wl, r0mat):

    # input parameters:
    # wl = emission wave length in m
    # r0mat = vectors pointing towards points of observation in cartesian
    # coordinates in m (3 x Ntheta x Nphi matrix)

    k0 = (2*pi)/wl          # emission wave number in 1/m
    w = k0*c                # emission angular frequency in 1/s
    eps1 = 1.               # dielectric constant medium 1 (vacuum)
    eps2 = epsAu(w)         # dielectric constant medium 2 (Au)

    # total distance between point of observation and beam impact point
    r = np.sqrt(r0mat[0, :, :]**2 + r0mat[1, :, :]**2 + r0mat[2, :, :]**2)

    # radial distance between point of observation and beam impact point
    R = np.sqrt(r0mat[0, :, :]**2 + r0mat[1, :, :]**2)

    # vertical distance between point of observation and beam impact point
    z = np.abs(r0mat[2, :, :])

    cosTheta = z/r          # sine of emission angle theta
    sinTheta = R/r          # cosine of emission angle theta

    # parallel wave vector component (conserved)
    Q = k0*sinTheta

    # perpendicular wave vector component in medium 1
    qz1 = sqrt(k0**2*eps1 - Q**2)

    # perpendicular wave vector component in medium 2

```



```

qz2 = sqrt(k0**2*eps2 - Q**2)

# electron momentum
q = sqrt(Q**2 + (w/v)**2)

D = (2j*e*Q/c)/(eps1*qz2 + eps2*qz1)
mu1 = (eps1*qz2 - eps1*w/v)/(q**2-k0**2*eps2) - (eps1*qz2 - eps2*w/v)/
      (q**2-k0**2*eps1)

# radial field component (exciting in-plane dipole moment)
ER = 1/(4*pi*eps0) * 1j*k0*cosTheta*D*mu1 * (exp(1j*k0*r)/r) * sinTheta
# vertical field component (exciting out-of-plane dipole moment)
Ez = 1/(4*pi*eps0) * 1j*k0*cosTheta*D*mu1 * (exp(1j*k0*r)/r) * cosTheta

return np.array([ER,Ez])

%% Definition of dipole emission (scattered field)
def E_scatt(wl,rSvec,rOmat,d):

    # input parameters:
    # wl = emission wave length in m
    # rSvec = vector pointing towards scattering dipole in cartesian
    #         coordinates in m (3 vector)
    # rOmat = vectors pointing towards points of observation in cartesian
    #         coordinates in m (3 x Ntheta x Nphi matrix)
    # d = spacing between adjacent dipoles in m

    k0 = (2*pi)/wl          # emission wave number in 1/m
    w = k0*c                # emission angular frequency in 1/s

    # duplicate rSvec for every point of observation to enable broadcasting
    # for fast computation
    rSrepmat = np.matlib.repmat(rSvec, np.shape(rOmat)[1], 1);
    rSrepmat2 = np.tile(rSrepmat, (np.shape(rOmat)[2], 1, 1));

    # vectors pointing to scattering dipole in m (3 x Ntheta x Nphi matrix)
    rSmat = np.transpose(rSrepmat2, (2, 0, 1));

    # vectors pointing from scattering dipole towards points of observation
    # in cartesian coordinates in m (3 x Ntheta x Nphi matrix)
    rDmat = rOmat-rSmat

    # total distance between points of observation and scattering dipole
    rd = np.sqrt(rDmat[0, :, :]**2 + rDmat[1, :, :]**2 + rDmat[2, :, :]**2);

    # total distance between points of observation and beam impact point
    r = np.sqrt(rOmat[0, :, :]**2 + rOmat[1, :, :]**2 + rOmat[2, :, :]**2);

    # radial distance between points of observation and beam impact point
    R = sqrt(rOmat[0, :, :]**2 + rOmat[1, :, :]**2)

    # vertical distance between points of observation and beam impact point
    z = sqrt(rOmat[2, :, :]**2)

    sinTheta = R/r          # sine of emission angle theta
    cosTheta = z/r          # cosine of emission angle theta

```

---

```

alpha0 = 3*d*sigma          # dipole effective polarization volume
phase0 = exp(1j*0)          # dipole scattering phase
E_inc = E_TR(wl,rSmat)      # incident electric field amplitude
P_rad = eps0*alpha0*E_inc[0] # induced radial polarization density
P_ver = eps0*alpha0*E_inc[1] # induced vertical polarization density

# radial field component induced by radial dipole moment
ER_rad = (mu0*w**2) * cosTheta/(4*pi*r) * P_rad * phase0 * exp(1j*k0*rd)
        * sinTheta;
# vertical field component induced by radial dipole moment
Ez_rad = (mu0*w**2) * cosTheta/(4*pi*r) * P_rad * phase0 * exp(1j*k0*rd)
        * cosTheta;

# radial field component induced by vertical dipole moment
ER_ver = (mu0*w**2) * sinTheta/(4*pi*r) * P_ver * phase0 * exp(1j*k0*rd)
        * sinTheta;
# vertical field component induced by vertical dipole moment
Ez_ver = (mu0*w**2) * sinTheta/(4*pi*r) * P_ver * phase0 * exp(1j*k0*rd)
        * cosTheta;

ER = ER_rad + ER_ver        # total radial field component
Ez = Ez_rad + Ez_ver        # total vertical field component

return np.array([ER,Ez])

%% Definition of total far-field intensity
def I_tot(k0,rOmat,rSmat,d,N):

    # input parameters
    # wl = emission wave length in m
    # rSmat = vectors pointing towards scattering dipoles in
    cartesian coordinates (3 x N matrix)
    # rOmat = vectors pointing towards points of observation in cartesian
    coordinates (3 x Ntheta x Nphi matrix)
    # d = spacing between adjacent dipoles in m
    # N = total number of scattering dipoles

    E_tot = E_TR(wl,rOmat)
    # initialize total electric field
    for n in range(0,N):
    # loop over N scattering dipoles
        rSvec = rSmat[:,n]
    # vector pointing towards scattering dipole n in cartesian coordinates
        E_tot = E_tot + E_scatt(wl,rSvec,rOmat,d)
    # add contribution of scattering dipole n to total electric field

    return (eps0*c/2) * (np.abs(E_tot[0, :, :])**2
        + np.abs(E_tot[1, :, :])**2)

%%
rSmat = np.zeros([3,N])
for k in range(0,N):
    rSmat[:,k] = np.array([x[k],y[k],hz])

```

```
###
thetaArray, phiArray = np.meshgrid(theta, phi, sparse=False, indexing='ij');
r0mat = np.array([sin(thetaArray)*cos(phiArray), sin(thetaArray)*sin(phiArray),
                  cos(thetaArray)])

kx = sin(thetaArray)*cos(phiArray)
ky = sin(thetaArray)*sin(phiArray)
I = I_tot(wl, r0mat, rSmat, d, N)
I = I/np.max(I)
```